Refined contour analysis of giant unilamellar vesicles

J. Pécréaux^{1,a}, H.-G. Döbereiner², J. Prost¹, J.-F. Joanny¹, and P. Bassereau¹

Received 13 January 2004 and Received in final form 11 March 2004 / Published online: 21 April 2004 – © EDP Sciences / Società Italiana di Fisica / Springer-Verlag 2004

Abstract. The fluctuation spectrum of giant unilamellar vesicles is measured using a high-resolution contour detection technique. An analysis at higher q vectors than previously achievable is now possible due to technical improvements of the experimental setup and of the detection algorithm. The global fluctuation spectrum is directly fitted to deduce the membrane tension and the bending modulus of lipid membranes. Moreover, we show that the planar analysis of fluctuations is valid for spherical objects, even at low wave vectors. Corrections due to the integration time of the video camera and to the section of a 3D object by the observation plane are introduced. A precise calculation of the error bars has been done in order to provide reliable error estimate. Eventually, using this technique, we have measured bending moduli for EPC, SOPC and SOPC: CHOL membranes confirming previously published values. An interesting application of this technique can be the measurement of the fluctuation spectra for non-equilibrium membranes, such as "active membranes".

PACS. 87.16.Dg Membranes, bilayers and vesicles – 05.40.-a Fluctuation phenomena, random processes, noise and Brownian motion – 07.60.Pb Conventional optical microscopes

1 Introduction

The mechanical properties of lipid membranes have been extensively studied over the last two or three decades [1] starting with the pioneering work by Helfrich [2–4]. These membranes are classically described as fluctuating 2dimensional sheets. Their elastic energy depends on two main parameters: the bending modulus κ and the tension σ [2,5]; this approach was recently supported by derivation of the energy based on the microscopic behaviour of the membrane, including the effect of the finite resolution of the microscope in measurement of the membrane area [6]. In particular, the bending modulus of membranes has been measured for systems of varying complexity (see [7] and references therein), from the simple one-component lipid to polymerised membranes [8,9] or membranes interacting with proteins [10]. Vesicles in the micrometer regime (also called "giant" vesicles) have been a popular system for measuring the fluctuations, since their size is suitable for direct observation using light microscope and for manipulation. Different techniques have been used over the years: micropipets [11], a sensitive technique for κ measurement but providing only an integrated measurement of the fluctuation spectrum⁽¹⁾, tether formation [12], elec-

tric fields [13], measurement of flickering, as in the case of red blood cells with direct methods [14] or more sophisticated ones [15–17]. Recently, Lee et al. also proposed an all-optical measurement of the bending modulus based on weak optical deformations of vesicles [18]. Unfortunately, none of these methods gives a direct measure of the fluctuation spectrum. From a detailed analysis of the contour of the vesicles, this spectrum was measured using more and more accurate methods: starting from only a portion of a contour [19-21], or detection of a piece of a planar membrane [22], the contour of the vesicle was later completely detected using the position of the intensity minimum in phase contrast [23–27], and eventually more precise methods [28,29], but the number of accessible modes with a reasonable signal-to-noise ratio remained in general limited. This is however sufficient in most cases for measuring κ and the spontaneous curvature of the membrane [30], or intermonolayer friction [31]. Nevertheless, for active membranes⁽²⁾, the fluctuation spectrum has been predicted to be modified by the activity of membrane proteins [32–34] and a more complex spectrum is expected. In this case, the difference between the spectrum of the passive membrane

¹ Physico-Chimie Curie, Institut Curie, Section Recherche, 11 rue Pierre et Marie Curie, 75231 Paris Cedex 5, France

² Biological Sciences, Columbia University, New York, NY 10027, USA

a e-mail: jacques.pecreaux@curie.fr

⁽¹⁾ In micropipet experiments the measured excess area uncrumpled by the aspiration can be calculated from the integral

of the fluctuation spectrum between a minimal ${\bf q}_\perp$ vector depending on the membrane tension and a molecular cut-off.

⁽²⁾ Membranes with incorporated proteins which can be activated by some source of energy, as ion channels or ion pumps.

and the active membrane should be more detectable at high mode (conversely, at small scale). In this perspective, we have developed a refined contour analysis, based on the Fourier analysis initially proposed by Döbereiner et al. [29] which provides a measurement of the fluctuation spectrum with a high resolution up to high-q modes and should be in principle extendable to non-equilibrium membranes. Moreover, the technique is not limited to spherical vesicles. In Section 2, we describe in detail the technical requirements to achieve a good spatial resolution and a good signal-to-noise ratio during the acquisition. The principles of our contour detection and of our analysis are given in Section 3, including the incorporation of the integration time and the fitting procedure. In Section 4, we present our measurements performed on classical lipid membranes, in order to test our technique, and compare them with those obtained by other groups with different techniques.

2 Methods

2.1 Vesicles preparation

We studied vesicles made up either of Egg PhosphatidylCholine (EPC), or Stearyl Oleoyl PhosphatidylCholine (SOPC) or a mixture of SOPC and Cholesterol (SOPC: CHOL) (Avanti Polar lipids) at a molecular ratio of 1:1. The lipid solutions in chloroform are kept under argon at $-20\,^{\circ}\text{C}$ in order to limit the oxidation of lipids and the formation of lysolipids. The classical electroformation technique originally developed by Angelova et al. [35, 36] and modified by Mathivet et al. [37] was used to prepare the Giant Unilamellar Vesicles (GUV): a thin layer of lipid solution is deposited on a conducting Indium Tin Oxide (ITO)-coated glass microscope plate (Thomson LCD). The complete evaporation of the solvent is achieved after one night under vacuum. A chamber made of two plates with the dry lipids deposited and a 1 mm Teflon spacer is built and filled with a 50 mM sucrose (Sigma-Aldrich) solution. The growth of the 5 to $50 \,\mu\mathrm{m}$ diameter vesicles is obtained after 3 hours at 1.1 V and 20 Hz. With this type of preparation, the majority of the vesicles are unilamellar and with very few defects (internal vesicles or thin tethers bound to the membranes). We only use freshly prepared vesicles to avoid any change of bending modulus due to vesicle aging [38,36].

2.2 Observation chamber preparation

The observation chamber consists of two cover slips separated by a parafilm spacer, which after heating to $150\,^{\circ}$ C, holds them together. The final inner thickness of the chamber is of the order of $500\,\mu\mathrm{m}$. In fact, due to the physical constraints associated with the use of an oil condenser and an immersion objective on our microscope, the total thickness of the chamber must be limited to 1 mm. It is initially filled with a slightly hyper-osmotic (typically 54 mM) glucose (Sigma-Aldrich) solution. Vesicles are then carefully

transferred from the formation chamber into the observation chamber using a glass pipet of 0.4 mm inner diameter (Vitrocom) with a gentle aspiration and injection (overpressure/depression in the pipets of the order of a few tens pascals). The small osmotic pressure difference between the vesicle interior and the bulk solution leads to more flaccid vesicles. Glucose and sucrose are classically used for phase contrast microscopy experiments to enhance the contrast of the vesicles because of their differences in refraction index (respectively, 1.3354 for the sucrose solution at 50 mM and 1.3342 for the glucose at 54 mM) and also for accelerating their sedimentation on the bottom of the chamber due to their slight difference in density (1001.6 kg/m³ for glucose solution at 54 mM and 1004.8 kg/m³ for sucrose at 50 mM). The sugar solutions are filtered beforehand to remove any particle which could perturb the contour recognition. Moreover, their osmotic pressure is also checked with an osmometer (Roebling). In order to avoid evaporation, the chamber is closed either with sealing paste (Vitrex) or mineral oil. Actually, the surface-to-volume ratio must be kept constant during the acquisition, and over longer periods; undesirable tethers, small buds or other shape transformations [27] could appear if the osmotic pressure varies. The temperature in the chamber is measured with a small thermocouple (type K, Farnell) and varies between 23 °C and 25 °C for all our experiments.

The observation of freely fluctuating vesicles requires the inhibition of their adhesion to the bottom glass substrate using the repulsive effect of grafted PEG molecules. For this reason, before assembling the chamber, the bottom cover slip is first cleaned with a mixture of sulfuric acid (70%) and hydrogen peroxide (30%), then coated with Mercaptopropyltrimethoxysilane (ABCR) in methanol, with a small amount of water and acetic acid. The second stage, is grafting PEG on silane by soaking a silanized cover glass in phosphate buffer saline (PBS) solution (pH = 7.4) of Methoxy-(PolyEthylene Glycol)_n-Maleimide (MW = 5000) (Shearwater Polymers) [39].

2.3 Experimental setup

The experimental setup has been optimized to provide the high contrast required for an accurate contour detection. For this reason, the phase contrast microscopy experiments are performed with an inverted microscope (Axiovert 135, Zeiss), equipped with an oil immersion condenser (Numerical Aperture (NA) = 1.4) and an oil immersion $100 \times$ objective (Plan-Apochromat, NA = 1.4, Zeiss), both with a high numerical aperture.

The light source is a 175 W xenon lamp (Eurosep). Its high power and its continuous spectrum allow for the use of coloured high-pass filters (for instance, yellow or red) necessary for some future experiments and still to keep a good contrast at a standard shutter aperture rate. Nevertheless, and even for pure lipid vesicles, we do not use white light, but a yellow filter to reduce the illumination spectrum because this improves the accuracy of the contour detection in phase contrast microscopy.

The image acquisition is performed using a digital CCD camera (Pulnix TM1040) for a good signal-to-noise ratio. Moreover, another advantage of a digital camera is to allow for a better spatial positioning of pixels, avoiding the jitter problem associated to the analogic-digital conversion when an analog camera is connected to a frame grabber, which creates a non-negligible error on the x-coordinates of the pixel. The images are acquired with a frame grabber (Matrox, Meteor II Digital) in a PC (biprocessor Intel Xeon 1.5 GHz machine) at 30 frames per seconds in progressive scan (non-interlaced) mode, but not stored as images files on the hard disk. The contour detection of the vesicles (see Sect. 3.1) is performed in real time and the contours are stored on the hard disk. An experiment includes several series of 2000 contours.

3 Detection and analysis procedures

3.1 Contour detection

In order to extract directly the fluctuation spectrum of the membranes from the contour analysis, we have first to detect the position of the membrane with a good precision, and reconstruct the full contour without artefacts. In the early approaches by Faucon et al. [24] or Sackmann et al. [23,27], the membrane position was assigned as corresponding to the minimum of intensity of the grey level profile and the contours were projected on spherical harmonics for analysis (the accuracy of the detection was, respectively, about 100 nm for Faucon et al., and up to 250 nm for Sackmann et al.). A more accurate detection was later developed by Döbereiner et al. using more precisely the sigmoid-shape of the grey level profile across the membrane in phase contrast microscopy [29] (see Fig. 1), leading to a spatial precision better than a pixel (accuracy of the detection 86 nm). More general shapes other than spherical could be analysed with a projection of the contours in polar coordinates $r(\theta)$ in Fourier series. This technique has been mainly used so far for a quantitative shape analysis of vesicles and a phase diagram determination [29,40], or for the physical measurement of the parameters of lipids [30], for which only the first four modes are required. Döbereiner's method [29] has been further improved in this work to achieve a better spatial resolution. Instead of using a single horizontal or vertical grey level profile and choosing the one that gives the largest slope, which leads to artefacts in the area where the contour is not close to a horizontal or vertical line, we use a weighted mean in four directions of the grey level profiles (see App. A). The detection is more robust and minimizes short-wavelength detection noise and backtracking. Eventually, the speed of the contour acquisition has been improved and 30 contours per second are treated and stored.

As previously, the principle of the detection is based on a well-known property of phase contrast microscopy: because of the refraction index difference between the interior of the vesicle and the bulk, the vesicle appears darker than the background and a halo is present on both sides of the contour (see [43], pp. 71-72; [44]). The microscope is

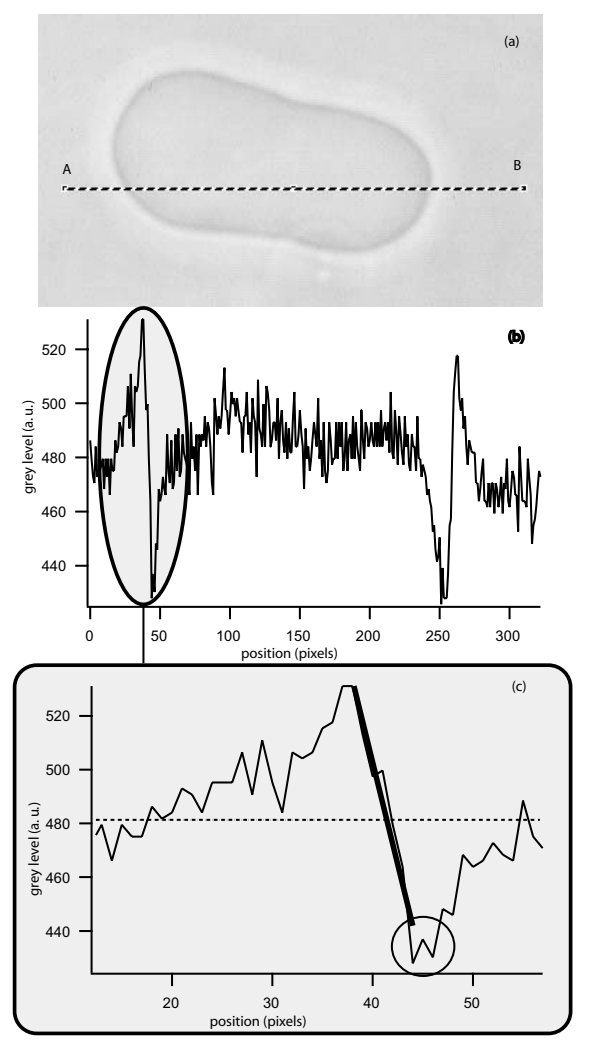


Fig. 1. (a) Image of a giant vesicle in phase contrast. The resolution of the photo is 11 pixels per micron. (b) Grey level profile along a horizontal line AB of the image (a) (length $29.4\,\mu\text{m}$). One can see two maxima in the slope corresponding to the position of both intersections with the contour. (c) Zoom in the profile (b) corresponding to the grey area. The profile is locally fitted by a line (continuous thick line); the dashed line corresponds to the mean grey level \bar{I}_0 of the section. The intersection of these two straight lines gives the estimated position of the membrane in the direction of the profile (for the next point algorithm). Note, inside the circle, that the minimum intensity in the halo can be split into two peaks due to the noise of detection; this can lead to accuracy loss if the membrane is localized by the minimum of intensity as in [41,42] or [27].

classically modeled by a "4f" system (Abbe's theory) [45]. The objective and ocular are represented by one lens, respectively; the sample is in the object focus plane of the first lens, the image focus of the first lens is coincident with the object focus of second lens; the image is detected in the image focus plane of the second lens. The phase contrast setup is of the Zernike type: in the focus plane, between the two lenses, a $\lambda/4$ phase plate of diameter a with an attenuation coefficient d is positioned. The plate is incorporated in a transparent disc of diameter b (see [44] for

further details), with (x', y') coordinates in object plane, and (x, y) coordinates in image plane. The transmittance t of the vesicle is given by

$$t(x', y') = \exp(i\phi_i) \quad \text{if} \quad x' > 0,$$

= \exp(i\phi_e) \quad \text{if} \quad x' < 0; \tag{1}

 $\phi_{\rm i}$ is the phase shift of rays diffracted by the interior of the vesicle, and $\phi_{\rm e}$ by the outside. This function models a refractive-index discontinuity due to the difference of sugar inside and outside the vesicle; here the vesicle is modeled only in one dimension as the boundary between two semi-infinite regions $(x' < x'_0 \text{ and } x' > x'_0)$ with different refractive indices. With $\Delta \phi = \phi_{\rm i} - \phi_{\rm e}$, according to [44], the intensity in the image plane is given by

$$I(x) = \left| d\cos\left(\frac{\Delta\phi}{2}\right) + \frac{2}{\pi}\sin\left(\frac{\Delta\phi}{2}\right) \right| \times \left[(id - 1)\operatorname{Si}(2\pi a(x - x_0)) - \operatorname{Si}(2\pi b(x - x_0)) \right]^2, (2)$$

where $\operatorname{Si}(z) = \int_0^z \frac{\sin(t)}{t} \mathrm{d}t$ is defined as the integral sine function, x is the abscissa in the image focal plane, and i is the imaginary symbol such that $i^2 = -1$. We have assumed that the membrane is at the position $x' = x'_0$ (parallel to the y'-axis). When x is close to x_0 , the corresponding position of the image of the membrane, equation (2), can be linearised and becomes

$$I(x) \underset{x \to 0}{\simeq} d^2 \cos^2 \left(\frac{\Delta \phi}{2}\right)$$

$$+4 \frac{d \cos\left(\frac{\Delta \phi}{2}\right) \sin\left(\frac{\Delta \phi}{2}\right) (-2\pi a + 2\pi b)}{\pi} (x - x_0). \quad (3)$$

This linear behaviour of the intensity close to $x=x_0$ is the basis of our recognition algorithm. Note that the membrane position does not correspond to the minimum of intensity.

An experimental example of a grey level profile of a vesicle across the membrane is given in Figure 1. We have decided to assign the position of the membrane as follows: the high-slope part of the sigmoid is fitted by a straight line and the average grey level \bar{I}_0 along a 30 pixel line centered on the sigmoid, is calculated. The position x_0 of the membrane is then fixed by the intersection of the fitted line, and the horizontal line $I = \bar{I}_0$. This procedure, taking advantage of the high slope of the section, provides a spatial resolution of a tenth of a pixel, better than the microscopy resolution [46], and thus a very good precision for the mode amplitude. Step by step as described in Appendix A, the next points of the contours are identified, and the contour can be fully detected. If the detected contour is not closed, the contour is discarded. Eventually, the contours are stored on the hard disk as a table containing the coordinates $(\tilde{x}_i, \tilde{y}_i)$ (see App. A for further details on this notation) for each point of the contours and time.

When all the contours have been detected, a last test on the contour length is performed to further discard defective contours. The length of the contours L is measured

as follows: \tilde{x}_i and \tilde{y}_i are the Cartesian coordinates of the contour, with i ranging from 1 to N, and the curvilinear distance ds_i is

$$ds_i = \sqrt{(\widetilde{x}_{i+1} - \widetilde{x}_i)^2 + (\widetilde{y}_{i+1} - \widetilde{y}_i)^2}.$$
 (4)

As the contour is closed, we have

$$ds_0 = ds_N = \sqrt{(\widetilde{x}_1 - \widetilde{x}_N)^2 + (\widetilde{y}_1 - \widetilde{y}_N)^2}. \tag{5}$$

The length L of the contour is obtained with

$$L = \sum_{i=1}^{N} ds_i \,. \tag{6}$$

We compute the time average of L, $\langle L \rangle$; thus, the length of each contour is compared to $\langle L \rangle^{(3)}$. Any contour longer or shorter than $\langle L \rangle$ by more than 10% is discarded. Actually, since the number of lipids in the bilayer is constant and the maximum excess area available is 8% for a zero-tension membrane with a bending rigidity of 4×10^{-20} J, the length of the contour cannot change to this extent for physical reasons.

3.2 Discrete Fourier analysis

The next stage is the transformation from Cartesian coordinates $(\tilde{x}_i, \tilde{y}_i)$ to polar coordinates (r_i, θ_i) . The center of the vesicles $(\tilde{x}_c, \tilde{y}_c)$ is defined as the average of the position of all points i in the contour, weighted by the sum of the distance between points i-1 and i, and between points i and i+1:

$$\widetilde{x}_c = \frac{1}{2L} \sum_{i=1}^{N} \widetilde{x}_i (ds_{i-1} + ds_i).$$
 (7)

A similar relation holds for \widetilde{y}_c . The transformation from $(\widetilde{x}_i, \widetilde{y}_i)$ to (r_i, θ_i) is then straightforward (see Eq. (C.4) and (C.5) in App. C for further details).

The last stage consists in the projection of these contours on Fourier series following an algorithm detailed in reference [47], pp. 140-156. The contour can be developed in Fourier modes,

$$r(\theta) = R \left(1 + \sum_{n=1}^{\infty} a_n \cos(n\theta) + b_n \sin(n\theta) \right)$$
 (8)

with R the radius of the contour defined as

$$R = \frac{1}{4\pi} \sum_{i=1}^{N} (r_i + r_{i+1}) \times (\theta_{i+1} - \theta_i).$$
 (9)

The ultimate goal of this analysis is a measure of the fluctuations of the position of the membrane with respect

 $^{^{(3)}}$ In the following, $\langle a \rangle$ denotes the time average value of a over a long period of time, and according to the ergodic hypothesis, the ensemble average over the possible states.

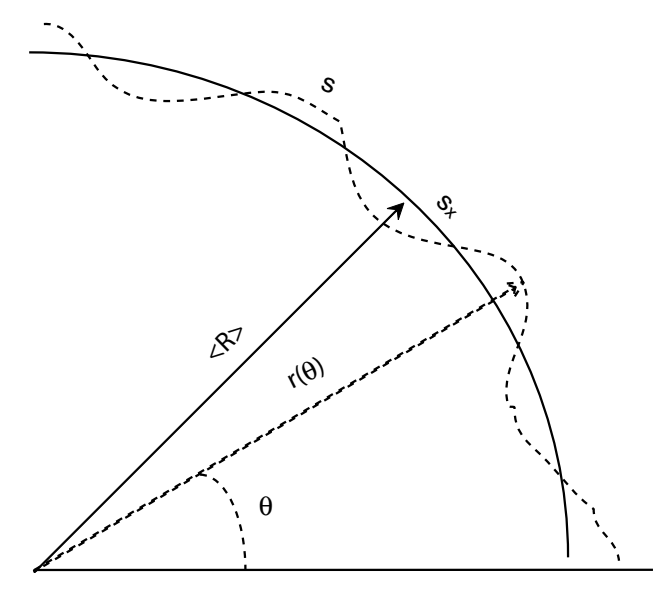


Fig. 2. Correspondence between the planar $(s_x, u(s_x))$ and polar (r, θ) coordinates systems. s is the curve abscissa along the contour (dashed line), s_x is the curve abscissa along the circle \mathcal{C} corresponding to the average position of the membrane (full line), and $u(s_x)$ is the local displacement of the membrane with respect to this circle \mathcal{C} . $s_x = \theta\langle R \rangle$ and $u(s_x) = R(\theta) - \langle R \rangle$.

to its average position; therefore, we must not measure the modulus $c_n = \sqrt{a_n^2 + b_n^2}$ but its fluctuations, i.e. $\langle c_n^2 \rangle - \langle c_n \rangle^2$.

Vesicle fluctuation spectra in spherical geometry were calculated by Milner and Safran [48]. As we are not interested in the shape of the vesicle but only in its fluctuations, we choose to work with the equations valid for a planar membrane. The errors due to curvature and closed topology of the membrane are important only for the first modes, and are nevertheless negligible compared to tension terms. The complete justification is given in Section 3.3. We will use below the fluctuation spectrum, calculated for planar membranes by Helfrich [49]:

$$\left\langle \left| u(\mathbf{q}_{\perp}) \right|^2 \right\rangle = \frac{k_{\rm B}T}{\sigma q_{\perp}^2 + \kappa q_{\perp}^4} \,,$$
 (10)

where $u(\mathbf{r}_{\perp})$ is the local displacement in the normal direction to the membrane (z-direction) with respect to its mean position. $\mathbf{q}_{\perp}=(q_x,q_y)$ is the wave vector corresponding to $\mathbf{r}_{\perp}=(x,y)$, the coordinates of the projection of a point of the membrane on the (x,y)-plane. σ is the membrane tension, κ the bending rigidity modulus, T the absolute temperature and $k_{\rm B}$ the Boltzmann constant.

Experimentally with microscopy experiments, only the fluctuations of the vesicle in the plane of its equator are accessible. We then measure

$$\left\langle \left| u(q_x, y=0) \right|^2 \right\rangle = \frac{k_{\rm B}T}{2\sigma} \left[\frac{1}{q_x} - \frac{1}{\sqrt{\frac{\sigma}{\kappa} + q_x^2}} \right].$$
 (11)

Only projections of the contours on discrete Fourier series can be measured whereas Fourier transforms are cal-

culated in the theory. This final transformation has also been introduced in our analysis. If R is quasi-constant for all contours of a given experimental run, we take as a reference $R \sim \langle R \rangle$ (mean over all the contours of the series). We show in the following that a surprisingly good description is provided by the choice of $a=2\pi\langle R \rangle$, since the membrane has a finite size; one can assume $u(z)^{(4)}$ (see Fig. 2) to be defined for $z \in \left[-\frac{a}{2}, \frac{a}{2}\right]$. This computation works also in non-spherical case, except for the first modes. We define the Fourier transform of u(z) as

$$\tilde{u}(q_x) = \frac{1}{\sqrt{a}} \int_{-a/2}^{a/2} u(z) \exp(-iq_x z) dz.$$
 (12)

Since discrete complex Fourier series are defined by

$$c_n = \frac{1}{\langle R \rangle} \frac{2}{a} \int_{-a/2}^{a/2} u(z) \exp\left(-i\frac{2\pi n}{a}z\right) dz, \qquad (13)$$

the transformation from the experimentally determined series $|c_n| = \sqrt{a_n^2 + b_n^2}$ to the Fourier transform $\tilde{u}(q_x)$ provided by the theory is easily obtained after the change of variable $q_x = \frac{n}{\langle R \rangle}$ and

$$\left\langle \left| \tilde{u}(q_x) \right|^2 \right\rangle = \frac{\pi \langle R \rangle^3}{2} \left(\left\langle \left| c_n \right|^2 \right\rangle - \left\langle \left| c_n \right| \right\rangle^2 \right).$$
 (14)

3.3 Comparison between the fluctuation spectrum for planar membrane and for spherical geometry

Figure 3 shows the comparison between the fluctuation spectra for a planar membrane $S_{\rm pl}(n)$ (see Eq. (15)) and for a spherical fluctuation spectrum $S_{\rm sh}(n)$ (see Eq. (16)). According to equation (11) and (14), the adimensional fluctuation spectrum for a flat membrane in discrete Fourier series is given by

$$S_{\rm pl}(n) = \frac{1}{\pi \langle R \rangle^3} \frac{k_{\rm B}T}{\sigma} \left[\frac{\langle R \rangle}{n} - \frac{1}{\sqrt{\frac{\sigma}{\kappa} + \frac{n^2}{\langle R \rangle^2}}} \right]. \tag{15}$$

To obtain the fluctuation spectrum in a spherical geometry, we use the equations derived in [24]. We transform the result in Fourier series in the equatorial plane as done in [23,27]. We then obtain the adimensional fluctuation spectrum:

$$S_{\rm sh}(n) = \sum_{n=p}^{n=n_{\rm max}} \frac{2n+1}{\pi} \frac{(n-p)!}{(n+p)!} \left(P_n^p(0)\right)^2 \frac{k_{\rm B}T}{\kappa \lambda_n}$$
 (16)

with $P_n^p(x)$ the associated Legendre polynomials as defined in reference [50], p. 694 and where

$$\lambda_n = n^2 (n+1)^2 - (2 - \bar{\sigma}) n(n+1) \tag{17}$$

⁽⁴⁾ z is the curve abscissa on the circle of radius $\langle R \rangle$ and u is the distance of the membrane to this circle.

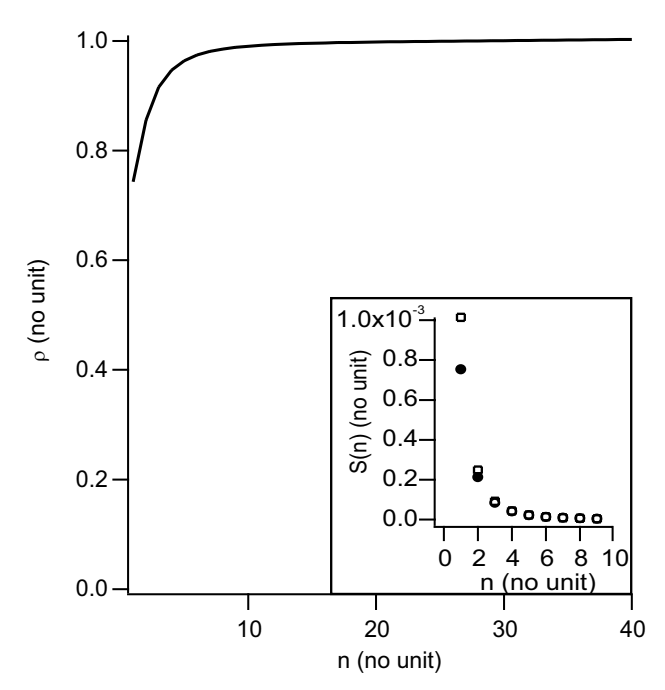


Fig. 3. Ratio ρ of the adimensional fluctuation spectrum in the planar case $S_{\rm pl}(n)$ (see Eq. (15)) over the adimensional fluctuation spectrum in spherical geometry $S_{\rm sh}(n)$ (see Eq. (16)). No relevant difference is observed except for the first 3 modes. Insert: fluctuation spectra, \Box for the spherical-geometry spectrum and \bullet for the planar-geometry one. The plot is displayed for a tension $\sigma = 10^{-8}\,{\rm N/m}$ and a bending modulus $\kappa = 22 \times 10^{-20}\,{\rm J}$, which are the values giving the largest gap between both geometries.

with $\bar{\sigma} = \frac{\sigma \langle R \rangle^2}{\kappa}$. We have followed the equations given in [24], and we have neglected the spontaneous curvature and made the hypothesis of quasi-spherical vesicles. In order to compare both spectra, we can compute eventually $\rho = \frac{S_{\rm pl}(n)}{S_{\rm sh}(n)}$.

The comparison of $S_{\rm pl}(n)$ and $S_{\rm sh}(n)$ leads us to conclude that there is no relevant difference for modes number larger than 5 (the error is equal to or smaller than the experimental error). Thus we can safely use the fluctuation spectrum for a planar membrane.

3.4 Camera integration time

As previously mentioned by other authors [38], the aperture time of the shutter of the camera introduces a further limitation in the analysis. Fluctuations with a lifetime shorter than the integration time of the camera are not correctly fitted. Consequently, the fluctuation lifetime $\tau_{\rm m}$ given by [51]

$$\tau_{\rm m}(\mathbf{q}_{\perp})^{-1} = \left(\frac{1}{4\eta q_{\perp}}\right) \left(\sigma q_{\perp}^2 + \kappa q_{\perp}^4\right) \tag{18}$$

and the integration time of the camera ($\tau=33\,\mathrm{ms}$) must be compared. If we denote q_\perp^C the q_\perp value for which $\tau_\mathrm{m}=$

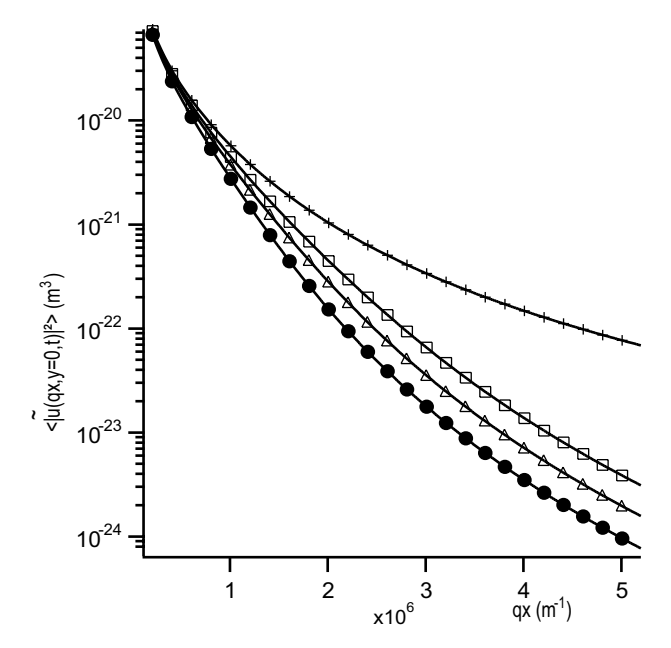


Fig. 4. Effect of the integration time on the fluctuation spectrum according to our theoretical analysis. The tension is $\sigma = 10^{-7} \, \mathrm{N/m}$ and the bending modulus $\kappa = 10 \times 10^{-20} \, \mathrm{J}$. From top to bottom, + corresponds to an infinitely short integration time, the three other ones correspond to integration times: $\Box \tau = 0.008 \, \mathrm{s}$, $\Delta \tau = 0.016 \, \mathrm{s}$ and $\bullet \tau = 0.03 \, \mathrm{s}$.

 τ , then

$$q_{\perp\sigma}^C = \frac{4\eta}{\sigma\tau} \tag{19}$$

in the tension-dominated regime $(\sigma q_{\perp}^2 \gg \kappa q_{\perp}^4)$, and

$$q_{\perp\kappa}^C = \sqrt[3]{\frac{4\eta}{\kappa\tau}} \tag{20}$$

in the bending-rigidity-dominated regime ($\sigma q_{\perp}^2 \ll \kappa q_{\perp}^4$).

The estimated order of magnitude for these wave vectors, with $\sigma=10^{-7}\,\mathrm{N/m},~\kappa=10^{-19}\,\mathrm{J},~\tau=33\,\mathrm{ms},~\eta=0.001\,\mathrm{kg/m\cdot s},$ gives similar values

$$q_{\perp\sigma}^C = 1.33 \times 10^6 \,\mathrm{m}^{-1}$$
 and $q_{\perp\kappa}^C = 1.1 \times 10^6 \,\mathrm{m}^{-1}$ (21)

We see in Figure 4, that the spectrum is already affected by this limitation for small q vectors, as previously mentioned by other authors [24,28] showing that this can absolutely not be neglected in the fitting procedure. The correction due to the integration time has been explicitly incorporated in our data processing [38,24] (see the details in App. B) and our data have been fitted using

$$\left\langle \left| \bar{u}(q_x, y = 0) \right|^2 \right\rangle = \frac{1}{\pi} \int_{-\infty}^{\infty} \frac{kT}{4\eta q_{\perp}} \tau_{\rm m} \frac{\tau_{\rm m}^2(q_{\perp})}{\tau^2} \times \left[\frac{\tau}{\tau_{\rm m}(q_{\perp})} + \exp\left(-\frac{\tau}{\tau_{\rm m}(q_{\perp})}\right) - 1 \right] \mathrm{d}q_y \,. \tag{22}$$

Méléard *et al.* [38] set up an experiment to bypass this difficulty using pulsed-light microscopy; however, this goes together with a severe deterioration of resolution, and noise increase due to speckle. Some tests varying integration time between 8 ms, 16 ms and 30 ms were achieved. Tension measurement is not very sensitive to integration time variations even if the correction is not included in the fit. This is expected since low- q_{\perp} modes only are dominated by tension (with long lifetime). On the contrary, the slope of the curve at high q_{\perp} is sensitive to time integration variations (see Fig. 4), and so are bending modulus measurements. The corrected fitting expression (Eq. (22)) gives results essentially independent of integration time in the above-mentioned range (results not shown).

Note that the rotational motion of the vesicle is smaller and can be neglected. The rotational relaxation time of a spherical vesicle of radius R is $T_{\rm r} = \frac{8\pi\eta R^3}{kT}$ [52]. In the bending-rigidity-dominated regime, for a fluctuation mode of wavelength q_{\perp} , $\frac{T_{\rm r}}{\tau_{\rm m}(q_{\perp})} = 2\pi(q_{\perp}R)^3\frac{\kappa}{kT}$. This is much larger than one (> 1000) for all the relevant experimental modes discussed in this paper $(n \geq 5)$.

3.5 Fitting procedure of the fluctuation spectrum

In our experiments, the values of κ and σ are deduced from the fit of the full plot of $\left\langle \left| \tilde{u}(q_x) \right|^2 \right\rangle = \frac{\pi \langle R \rangle}{2} (\left\langle \left| c_n \right|^2 \right\rangle - \left\langle \left| c_n \right| \right\rangle^2)$ versus $q_x = \frac{n}{\langle R \rangle}$, using equation (22). This is the main difference with previous papers, where κ is generally calculated as the average of values calculated for each mode, discarding the first modes and the last ones [24,28].

For reasons already exposed in Section 3.2, the five first modes are not fitted. The fit should be also limited in theory at high-q mode by the pixelisation of the images; fluctuation with a wavelength shorter than pixel size (90 nm) and the optical resolution are not detected. The corresponding high-q cut-off is of the order of a few $10^7 \,\mathrm{m}^{-1}$, higher than what is experimentally accessible.

We have quantified experimentally the noise due to the camera, to the frame grabber and also to the limited precision with floating point computations. A drop of ink dried on glass cover slip has been used as a model for a fixed object in the focal plane. We have measured $\langle |u(q_x,y=0,t)|^2 \rangle < 10^{-22}\,\mathrm{m}^3$ for all spectra. Consequently, this value fixes the lower limit for our detection and every fluctuation amplitude smaller than this is discarded.

The pixelisation of the image has, in addition, general consequences. First, the pixelization of the lateral membrane position sets a lower value for the detection of fluctuation wavelength ($\simeq 4\,\mathrm{pixel}$). Second, the pixelization in the direction orthogonal to the membrane leads to additional and more subtle limitations. As shown in Section 3.1, the profile analysis of the transmitted image allows to detect the membrane position within a tenth of the pixel size. This means that the membrane position in this direction, has a random component of a tenth of a pixel. For a biological polymer, it has been shown [53] that this noise introduces a component in the fluctuations

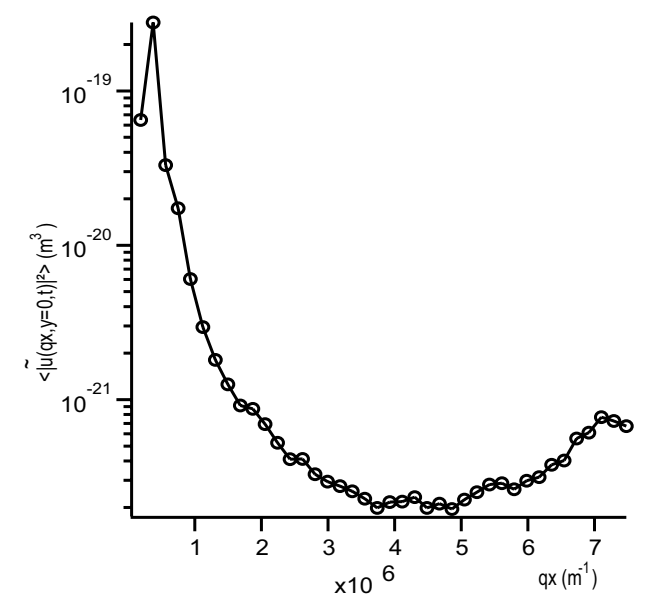


Fig. 5. Variation of the fluctuation amplitude $\langle \tilde{u}^2(q_x) \rangle$ with wave vector q_x for a SOPC: CHOL vesicle over the full q_x -range. A high-q increase of $\langle |\tilde{u}(q_x)|^2 \rangle$ is observed due to the finite uncertainty in the contour determination as discussed in the text, starting here at $q = 4 \times 10^6 \, \mathrm{m}^{-1}$.

increasing with the mode number and dominant at high n. A similar analysis can be done for a membrane. In fact, our definition of the fluctuations can be related to the variance of the amplitude c_n . The noise due to the detection contributes to the fluctuations, according to the expression:

$$\langle |u_{\text{mes}}(q_x, y=0)|^2 \rangle = \langle |u_{\text{th}}(q_x, y=0)|^2 \rangle + \frac{\pi \langle R \rangle^3}{2} \text{var}(c_n),$$
(23)

where $u_{\rm mes}$ corresponds to the measured fluctuations and $u_{\rm th}$ to the theoretical value (deduced from the theoretical expression of the fluctuation spectrum). The last term has been computed for a series of experimental points in Appendix C and is the variance of c_n computed as

$$var(c_n) = \frac{\sum_{l} (c_n^l - \bar{c}_n)^2}{L - 1},$$
(24)

where l indexes the L contours and \bar{c}_n is the mean value of c_n^l over the L contours. The variation with n cannot be extracted in a straightforward manner, but the variance increases with n, leading to an increase of the fluctuations with n as observed experimentally in Figure 5. This contribution of the noise due to the fluctuation spectrum should be in fact a general consequence of the discrete detection of the contours. However, the crossover between the decreasing fluctuation spectrum at small wave vector and the increasing contribution of the noise due to the detection at high q_{\perp} will depend directly on the error on the detection. This is an additional argument for the development of a protocol optimizing the precision of the detection of the contour.

These two effects are in fact the main limitations of the analysis at high q vectors. Practically, the fits are

restricted to amplitudes $\langle |\tilde{u}(q_x)|^2 \rangle$ larger than $10^{-22}\,\mathrm{m}^3$ and before a levelling of the spectrum (for instance, in Fig. 5, the fit is limited to $q_{\perp} < 4 \times 10^6 \mathrm{m}^{-1}$).

3.6 Precision of the fit

The uncertainties in the mean-square amplitude determination have been calculated according to a procedure described in Appendix C. The standard deviation for the amplitudes $\langle |\tilde{u}(q_x)|^2 \rangle$ has been precisely derived and after fitting, we obtain the standard deviation for the tension and bending modulus, from the standard deviation for the position of the experimental points defining the contour; then, it is clear that it is essential to have a high precision on the contour position to obtain precise results.

This calculation allows to weigh each point $(q_x, \langle |\tilde{u}(q_x)|^2 \rangle)$ with its precise error bar during the fitting procedure of the fluctuation spectrum, instead of allocating the same value to every point that overestimates the error for first modes (low q_x) and underestimates it for high modes (high q_x).

We explicitly incorporate the precision on the amplitudes of the modes in the calculation of the error bars. This can lead to error bars apparently similar to or higher than what is published usually, but most of the time, the authors produce only the χ^2 of the fits as a measure of the precision of their data, which is obviously an underestimation.

3.7 Effect of gravity

We have estimated the gravitational effect on our measurements. Due to the density difference between the interior and the exterior of the vesicle, it tends to sediment on the bottom of the chamber and be deformed. This effect is particularly important for the shape analysis [29] as it affects mostly the first deformation modes. Experimentally, we choose to use moderate sugar concentrations to limit this problem, although a better optical contrast can be achieved with higher concentrations.

Intuitively, the larger vesicles are more deformed than the smaller ones. Henriksen *et al.* [54] have calculated a criterion for the maximal size of the vesicle below which the gravity effect can be neglected. Neglecting spontaneous curvature, gravity is negligible if

$$g_0 \lesssim (12 + \Sigma) \tag{25}$$

with $g_0 = \Delta \rho g R^4/\kappa$ and $\Sigma = \frac{\sigma R^2}{\kappa}$. This condition is equivalent to the following condition for the radius:

$$R \lesssim R_{\text{max}} = \sqrt{\frac{\frac{\sigma}{\kappa} + \sqrt{\left(\frac{\sigma}{\kappa}\right)^2 + \frac{4\Delta\rho g}{\kappa}} 12}{\frac{2\Delta\rho g}{\kappa}}}.$$
 (26)

For our vesicles, the bending modulus is larger than or equal to $\kappa = 6.4 \times 10^{-20} \text{J}$, and the tension is typically

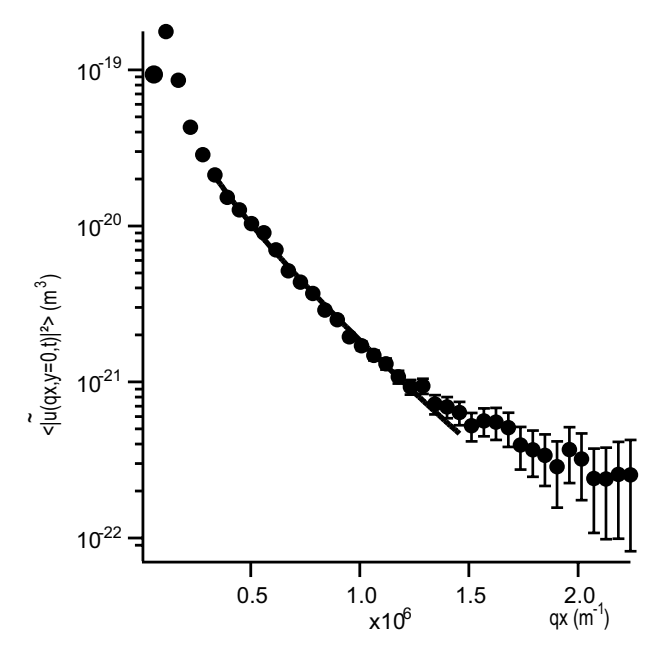


Fig. 6. Variation of the amplitude of the fluctuations $\langle |\tilde{u}(q_x)|^2 \rangle$ versus the wave vector q_x for a SOPC vesicle. Error bars have been computed according to the discussion of Appendix C. The solid line corresponds to the fit of the data using equation (22), with $\sigma=1.74\times 10^{-7}\,\mathrm{N/m}$ and $\kappa=9.44\times 10^{-20}\,\mathrm{J}$.

larger than or equal to $\sigma=2\times 10^{-8}\,\mathrm{J~m^{-2}}$. For 50 mM sucrose and glucose solutions, $\Delta\rho=\rho_{\mathrm{in}}-\rho_{\mathrm{out}}=1005.0-1002.0=3\,\mathrm{kg/m^3}$ [55]. We obtain $R_{\mathrm{max}}=25\,\mu\mathrm{m}$. The selected vesicles for our analysis have a radius ranging between 2.5 and 25 $\mu\mathrm{m}$; gravity therefore should have no effect on our measurements.

4 Results and discussion

In order to test our technique, we have measured the bending rigidity modulus κ and the tension σ for different lipid compositions: EPC, SOPC and SOPC: CHOL (1:1), for which data exist in the literature. We have obtained spectra analysable for the first 20 to 30 modes (in discrete Fourier representation). We have used our expression based on a fluctuation spectrum in a planar geometry and taking into account the camera integration time (Eq. (22)), with the different limitations described above for the fit of our data. The fit quality is excellent, as displayed in a typical example (Fig. 6). We discard the first five modes, as explained in Section 3.2.

In order to measure the error bar for each measurement, we have first assumed that the standard deviation for the position of contour points is 0.1 pixel. This corresponds to the error bars on the mode amplitudes plotted in Figure 6. For each experiment, the standard deviation is then calculated according equation (C.22) in Appendix C. It highly depends on the size of the vesicle (the precision increases with the vesicle size; as much as possible, large

Table 1. Bending modulus of EPC, SOPC, SOPC : CHOL.

Lipid	Bending modulus $\kappa (10^{-20} \mathrm{J})$	Standard deviation $\sigma_{\kappa} (10^{-20} \mathrm{J})$
EPC	4.25	0.87
SOPC	12.6	2.6
SOPC: CHOL	29.6	3.3

vesicles have been selected) and on the quality of the fit. We have tested the reproducibility of our measurements. The acquisition has been performed sequentially on the same vesicle: 2000 contours were acquired, and after a 10 s pause another series of contours was stored, and so on. This procedure was repeated 10 times. Curves for different series are found superimposed (data not shown).

In these conditions, for each vesicle, we have computed the average value of the bending modulus $\bar{\kappa}$ over several series of contours, weighted by the inverse of standard deviation. We have measured M series of contours for a vesicle indexed by i, with a bending modulus κ^i and a standard deviation for this value of σ^i_{κ} . We computed the weighted mean of the bending modulus as

$$\bar{\kappa} = \frac{\sum_{i=1}^{M} \frac{\kappa^i}{\left(\sigma_{\kappa}^i\right)^2}}{\sum_{i=1}^{M} \frac{1}{\left(\sigma_{\kappa}^i\right)^2}}.$$
(27)

Under these conditions, measurements with the highest errors contribute less. A distribution of κ values has been measured for a series of typically 10 vesicles.

The mean κ value for every lipid composition is eventually deduced as the average value over the vesicles, weighted as above. The values found for the bending rigidities are reported in Table 1. These results are in good agreement with data previously obtained with different techniques (see Tab. 2 for comparison). The error bars have not been reported in Table 2 on purpose, as the methods of calculation are quite different among the papers and most often underestimate the errors. Besides, our experiment aimed at measuring fluctuation spectra rather than bending moduli; therefore we obtained a lower accuracy than recent experiments specially designed for κ measurement [30].

The fits of our data produce values of the tension ranging between $2 \times 10^{-8} \,\mathrm{N/m}$ and $10^{-6} \,\mathrm{N/m}$. This tension range is similar to typical values found by other authors with spectral-analysis methods [27,24] and to the lowest tensions accessible in micropipet experiments [11].

5 Conclusion

The method of contour analysis presented here provides a direct measurement of the fluctuation spectrum of vesicles. Although we have given a detailed analysis in the case of spherical vesicles, it is not restricted to that case:

Table 2. Bending modulus of EPC, SOPC, SOPC : CHOL found by other authors.

Lipid	Bending modulus $\kappa (10^{-20} \text{ J})$	Technique	Ref.
EPC EPC EPC EPC EPC	10-20 4-5 11.5 8 2.5 6.6	Correlation functions Vesicle contour analysis Vesicle contour analysis Contour analysis Electric field Vesicle contour analysis	[19] [24] [28] [22] [13] [41]
SOPC SOPC SOPC SOPC SOPC SOPC	20 9 14.4 12.7 18.1 12.7	Tethers on vesicle Micropipets Vesicle contour analysis Vesicle contour analysis Vesicle contour analysis Vesicle contour analysis	[12] [11] [27] [41] [42] [30]
SOPC: CHOL ratio 1:1 SOPC: POPS: CHOL ratio 39.2:0.8:60	24.6 36	Micropipets Tethers on vesicle	[11] [56]

high-q modes do not depend on the actual shape. The vesicles fluctuation spectrum has been measured for classical lipid compositions, EPC, SOPC and SOPC : CHOL. We have adapted the theoretical expression of the fluctuation spectrum for planar membranes to our experimental conditions, and obtained a very good fit of our data sets with this expression. The bending rigidity moduli deduced from these fits are in very good agreement with previous data from other groups, and the membrane tensions range from 2×10^{-8} N/m to 10^{-6} N/m, which is reasonable. We have improved the contour analysis technique in two ways. First, the fluctuation spectrum can be fitted up to high mode numbers and not only for the first modes as in references [15, 24, 28, 29]. Second, the precision of the experiment is high enough to allow for a real fit of the spectrum by a theoretical equation and not only a derivation of the bending modulus by an average of values found for each mode (excluding first modes and high modes) as in references [27,23,20,21,19]. This is the first step for measuring more complex fluctuation spectra as expected, for instance, for non-equilibrium vesicles. New spectra with different scaling laws of the wave vector have been predicted for active membranes [32,33]. With our new development of the spectral analysis, we should be able to measure directly the spectra of active membranes (membranes containing ion pumps such as the light-activated proton pump, the bacteriorhodopsin [34]) and not only an effective temperature.

We would like to thank P. Girard for valuable help in computations. This work was supported by the association Procope and an ACI (Action Concertée Incitative) "Physico-Chimie de

la matière complexe" of the CNRS (Centre National de la Recherche Scientifique). J. Pécréaux was supported by DGA (Délégation Générale à l'Armement) and ARC (Association pour la Recherche contre le Cancer).

Appendix A. Principle of the contour detection

We detail here the consecutive steps for our contour detection protocol. We have first to find one point of the contour. A horizontal section through the diameter of the vesicle is performed giving the grey levels profile. Over an interval of 11 points, the shape of the profile is linearly fitted and the slope measured (see Fig. 1). This operation is repeated for each point along the section. The point of the series giving the highest slope is assigned to be the first point of the contour $(\tilde{x}_{-10}, \tilde{y}_{-10})$ (see Fig. 1). Actually, the first points are discarded to allow for the algorithm to have "a few points delay" to find very well the membrane position and because the general direction of the contour is arbitrarily fixed for the first points (see below); we discard typically ten points. In the following, we denote by $(\tilde{x}_i, \tilde{y}_i)$ the position of the membrane (corresponding to fractions of pixels) and (x_i, y_i) the pixel position (with integer values).

The principle to find the next point is the following (see Fig. 7). It must be applicable to any point of the contour. For this reason, we must, for each point, explore the horizontal and vertical axes (x and y) and the diagonal axes (v and w) in the vicinity of the origin to find the next point in the different sections. We give here only the details of the detection on the x-axis; this procedure is reproduced for the other 3 axes. We name the initial pixel position (x_i, y_i) . Let us assume that (x_i, y_i) is the origin of a local system of coordinates. The orientation in the ydirection (positive or negative) is fixed by the orientation of the past 10 points (for the first 10 points, it is arbitrarily fixed in the positive direction). For this proof, we suppose that the position of the next point corresponds to $y > y_i$. The horizontal profile through the point $(x_i, y_i + 1)$ is plotted. The x value \bar{x}_i corresponding to the intersection of the horizontal line representing the mean grey level value over 30 points centered around $(x_i, y_i + 1)$, and the fitted line on the 11 points of the grey level profile centered around $(x_i, y_i + 1)$ is computed (see Fig. 1 (c)). The slope S_i^x of the fitted line is recorded. The same analysis is done along the vertical axis for $(x_i + 1, y_i)$ and the point (x_i+1,\bar{y}_i) corresponding to a slope S_i^y is measured. The equivalent analysis is further performed for the diagonal axes (v, w), taking into account that the spacing between the discrete points is increased by a $\sqrt{2}$ factor. This provides 2 sets of 4 values, one along x and one along y. The position $(\tilde{x}_{i+1}, \tilde{y}_{i+1})$ of the membrane is eventually fixed by the average of the 4 values weighted by the different

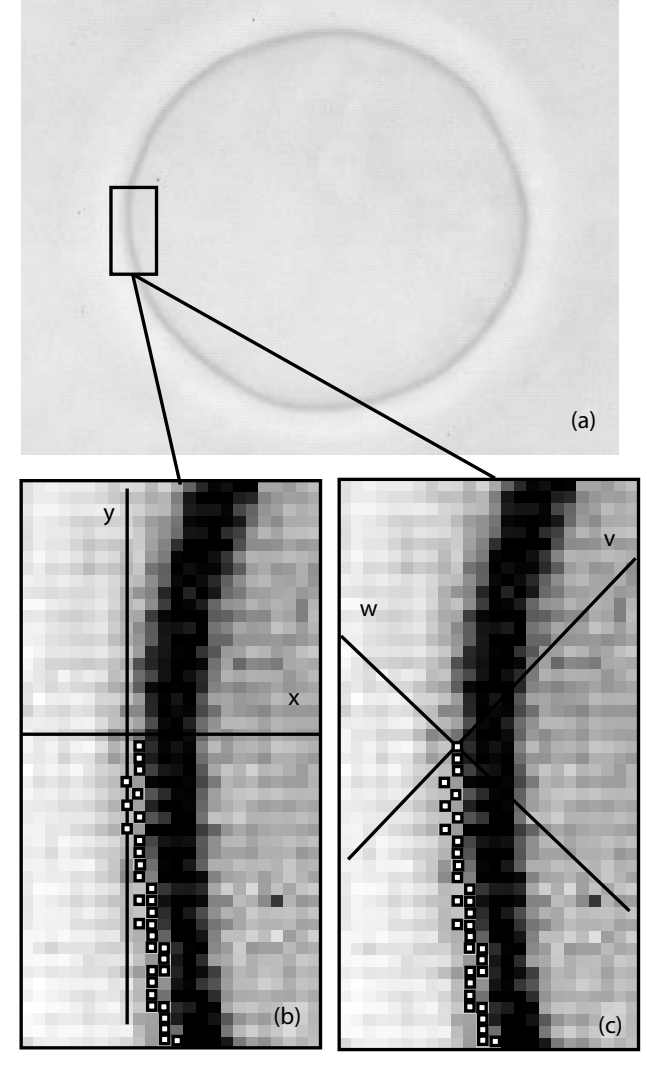


Fig. 7. Principle of contour detection. Zoom on the contour of the vesicle (a). The contrast has been enhanced for clarity. Pixels marked with a white square with black contour are the already detected points of the contour of the vesicle. The next point is searched along the x and y axes (b) and v and w axes (c).

slopes:

$$\tilde{x}_{i+1} = \left[S_i^x(x_i \pm 1) + S_i^y(\bar{x}_i) + S_i^v(\pm\sqrt{2}/2 - \bar{w}_i/\sqrt{2}) \right] + S_i^w(\mp\sqrt{2}/2 + \bar{v}_i/\sqrt{2}) \left] \frac{1}{S_i^x + S_i^y + S_i^v + S_i^w}, \tag{A.1}$$

$$\tilde{y}_{i+1} = \left[S_i^x(\bar{y}_i) + S_i^y(y_i \pm 1) + S_i^v(\pm\sqrt{2}/2 + \bar{w}_i/\sqrt{2}) + S_i^w(\pm\sqrt{2}/2 + \bar{v}_i/\sqrt{2}) \right] \frac{1}{S_i^x + S_i^y + S_i^v + S_i^w}.$$
(A.2)

To proceed to the next point (x_{i+2}, y_{i+2}) , we assign the membrane position $(\tilde{x}_{i+1}, \tilde{y}_{i+1})$ to a position on the pixel grid (x_{i+1}, y_{i+1}) by taking the pixel closest to $(\tilde{x}_{i+1}, \tilde{y}_{i+1})$

excluding the pixel (x_i, y_i) , or taking a point in the direction of the tangent of the contour defined by the last 10 points, or using the highest-slope direction to determine the next point. This operation of finding a next point is repeated 700 to 2000 times, the number of pixels in a contour of a vesicle depending on its size, to reach a quasi-superposition (within pixel accuracy) of the last point and the point (x_0, y_0) .

Appendix B. Effect of the integration time

The Langevin equation for a fluctuating membrane is given by [34,51]

$$\frac{\partial u(\boldsymbol{q}_{\perp},t)}{\partial t} + \tau_{\mathrm{m}}(\boldsymbol{q}_{\perp})^{-1} u(\boldsymbol{q}_{\perp},t) = \lambda_{\mathrm{p}} \left[f_{\mathrm{th}}(\boldsymbol{q}_{\perp},t) + \frac{1}{2\pi\eta\lambda_{\mathrm{p}}} \int \frac{\boldsymbol{f}_{h}(\boldsymbol{q},t) \cdot \boldsymbol{k}}{q^{2}} \mathrm{d}q_{z} \right], (B.1)$$

where

$$\tau_{\rm m}(\boldsymbol{q}_{\perp})^{-1} = \left(\lambda_{\rm p} + \frac{1}{4\eta q_{\perp}}\right) \left(\sigma q_{\perp}^2 + \kappa q_{\perp}^4\right) \tag{B.2}$$

is the relaxation rate of the membrane, $\lambda_{\rm p}$ the permeation of the membrane, η the viscosity of the solvent, f_h is the volume thermal noise and $f_{\rm th}$ the surface thermal noise and $q_{\perp} = \|q_{\perp}\|$.

In our system, $\lambda_{\rm p} \simeq 10^{-12}\,{\rm m}^3/{\rm Ns},~\eta \simeq 0.001\,{\rm kg/m\cdot s},$ and $q_{\perp} < 5 \times 10^6\,{\rm m}^{-1}$, then the viscous relaxation should be dominant in our experimental q-range:

$$\lambda_{\rm p} \ll \frac{1}{4\eta q_{\perp}}.$$
 (B.3)

We use the following notations for the different average values of the variable a: $\langle a \rangle$ being the ensemble average over possible states and \bar{a} the average over the integration time. The correlation function is then given by

$$\langle |u(\mathbf{q}_{\perp}, t)u(\mathbf{q}'_{\perp}, t')| \rangle = 4\pi^{2} \frac{kT}{4\eta q_{\perp}} \delta(\mathbf{q}_{\perp} + \mathbf{q}'_{\perp})$$
$$\times \tau_{\mathrm{m}}(q_{\perp}) \exp\left(-\frac{t' - t}{\tau_{\mathrm{m}}(q_{\perp})}\right)$$
(B.4)

(we have removed a transient term). The average of the correlation function over the period of integration on the CCD τ leads to

$$\langle |\bar{u}(\boldsymbol{q}_{\perp},t)\bar{u}(\boldsymbol{q}'_{\perp},t)|\rangle = \frac{2}{\tau^{2}} \int_{t_{1}=t}^{t_{1}=t+\tau} \int_{t_{2}=t_{1}}^{t_{2}=t+\tau} 4\pi^{2} \frac{kT}{4\eta q_{\perp}} \delta(\boldsymbol{q}_{\perp} + \boldsymbol{q}'_{\perp}) \times \tau_{\mathrm{m}}(q_{\perp}) \exp\left(-\frac{t_{2}-t_{1}}{\tau_{\mathrm{m}}(q_{\perp})}\right) \mathrm{d}t_{2} \mathrm{d}t_{1}$$
(B.5)

and eventually to

$$\langle |\bar{u}(\boldsymbol{q}_{\perp},t)\bar{u}(\boldsymbol{q}'_{\perp},t)|\rangle = 8\pi^{2} \frac{kT}{4\eta q_{\perp}} \delta(\boldsymbol{q}_{\perp} + \boldsymbol{q}'_{\perp}) \times \tau_{m}$$
$$\times \frac{\tau_{m}^{2}(q_{\perp})}{\tau^{2}} \left[\frac{\tau}{\tau_{m}(q_{\perp})} + \exp(-\frac{\tau}{\tau_{m}(q_{\perp})}) - 1 \right]. \quad (B.6)$$

The correction factor due to the integration is similar to the factor calculated by Faucon *et al.* [24]. If we integrate to the calculation the projection on the equatorial plane, we obtain the following integral:

$$\langle |\bar{u}(q_x, y = 0, t)|^2 \rangle = \frac{1}{\pi} \int_{-\infty}^{\infty} \frac{kT}{4\eta q_{\perp}} \tau_{\rm m} \frac{\tau_{\rm m}^2(q_{\perp})}{\tau^2} \times \left[\frac{\tau}{\tau_{\rm m}(q_{\perp})} + \exp\left(-\frac{\tau}{\tau_{\rm m}(q_{\perp})}\right) - 1 \right] \mathrm{d}q_y \,. \tag{B.7}$$

It has been calculated using the Gauss-Laguerre quadrature, or the Romberg integration methods with the algorithms provided in reference [47], pp. 140-156. These algorithms are not directly applied on the integral (B.7), but with the changed variables described below in the case of Romberg method:

$$\xi = \frac{\tau}{\tau_{\rm m}(\mathbf{q}_{\perp})} - \frac{\tau}{\tau_{\rm m}(q_x, q_y = 0)}$$

$$= \frac{\tau 4\eta \sqrt{q_x^2 + q_y^2}}{\sigma(q_x^2 + q_y^2) + \kappa(q_x^2 + q_y^2)^2} - \frac{\tau 4\eta \sqrt{q_x^2}}{\sigma(q_x^2) + \kappa(q_x^2)^2}. \quad (B.8)$$

Then with

$$\xi_0 = \frac{\tau}{\tau_{\rm m}(q_x, q_y = 0)} = \frac{\tau 4\eta \sqrt{q_x^2}}{\sigma(q_x^2) + \kappa(q_x^2)^2}$$
 (B.9)

and $\widetilde{\xi} = \xi + \xi_0$, we have

$$\alpha = \left[\tau \left[\tau^2 \sigma^3 + 216\kappa \tilde{\xi}^2 \eta^2 + 12\sqrt{3}\tilde{\xi}\eta \sqrt{\frac{\tau^2 \sigma^3 + 108\kappa \tilde{\xi}^2 \eta^2}{\kappa}}\kappa\right]\right]^{1/3}, \quad (B.10)$$

$$q_y = \frac{1}{3} \left[\frac{3\alpha}{\kappa \tau} + \frac{3\sigma^2 \tau}{\kappa \alpha} - 3 \frac{3\kappa q_x^2 + 2\sigma}{\kappa} \right]^{1/2}.$$
 (B.11)

We have eventually

$$\langle |\bar{u}(q_x, y = 0, t)|^2 \rangle = \frac{2kT}{\pi} \times \int_0^\infty \frac{1}{\tilde{\xi}^3} \left(\exp(-\tilde{\xi}) + \tilde{\xi} - 1 \right) \times \frac{\mathrm{d}\xi}{q_y \left(3\kappa(q_x^2 + q_y^2) + \sigma \right)}, \quad (B.12)$$

to which the algorithms are applied.

In the case of Gauss-Laguerre quadrature, the new variable is

$$\zeta = \frac{q_y}{q_z},\tag{B.13}$$

leading to

$$\tau_{\rm m} = \frac{4\eta q_x \sqrt{1+\zeta^2}}{\sigma q_x^2 (1+\zeta^2) + \kappa q_x^4 (1+\zeta^2)^2},$$
 (B.14)

$$\langle |\bar{u}(q_x, y = 0, t)|^2 \rangle = \int_0^\infty \frac{2}{\pi} \frac{kT\tau_{\rm m}^3}{\tau^2} \frac{1}{4\eta q_x \sqrt{1 + \zeta^2}} \times \left(\frac{\tau}{\tau_{\rm m}} + \exp\left(-\frac{\tau}{\tau_{\rm m}}\right) - 1\right) q_x d\zeta.$$
 (B.15)

Appendix C. Uncertainty calculation

We assume that the uncertainty on the position $(\tilde{x}_i, \tilde{y}_i)$ of one point of the contour can be modeled by a Gaussian, with zero mean value (ignoring systematic errors) and variance σ_0^2 . First, we compute the center of the contour, $(\widetilde{x}_c, \widetilde{y}_c)$ by

$$\widetilde{x}_c = \frac{1}{2L} \sum_{i=1}^{N} \widetilde{x}_i \times (ds_{i-1} + ds_i)$$
 (C.1)

and idem for \widetilde{y}_c , where

$$S = \sum_{i=1}^{N} s_i \quad \text{and} \quad s_i = \sqrt{(\widetilde{x}_{i+1} - \widetilde{x}_i)^2 + (\widetilde{y}_{i+1} - \widetilde{y}_i)^2}.$$

The error on \tilde{x}_c is then a Gaussian of zero-mean and variance σ_0^2 , and the same on y_c . We will now compute the centered coordinates, $\hat{x}_i = \tilde{x}_i - \tilde{x}_c$ and $\hat{y}_i = \tilde{y}_i - \tilde{y}_c$. The variance of \hat{x}_i is then

$$\sigma_{\hat{x}_i} = \sigma_{\hat{y}_i} = \sqrt{2}\sigma_0. \tag{C.3}$$

The next step is the transformation of Cartesian coordinates to polar coordinates. For the point (\hat{x}_i, \hat{y}_i) , polar coordinates are (r_i, θ_i) , where

$$r_i = \sqrt{\hat{x}_i^2 + \hat{y}_i^2} \tag{C.4}$$

and

$$\theta_i = \begin{cases} \arctan \frac{\hat{y}_i}{\hat{x}_i} & \text{if} \quad \hat{x}_i > 0, \\ \arctan \frac{\hat{y}_i}{\hat{x}_i} + \pi & \text{if} \quad \hat{x}_i < 0 \text{ and } \hat{y}_i > 0, \\ \arctan \frac{\hat{y}_i}{\hat{x}_i} - \pi & \text{if} \quad \hat{x}_i < 0 \text{ and } \hat{y}_i < 0. \end{cases}$$
(C.5)

The standard deviations are given by, according to reference [57], pp. 532-537,

$$\sigma_{r_s} = \sqrt{2}\sigma_0 \tag{C.6}$$

and

$$\sigma_{\theta_i} = \frac{\sqrt{2}\sigma_0}{r_i} \tag{C.7}$$

and covariances

$$cov(r_i, \theta_j) \simeq \delta_{ij} \frac{2\sigma_0^2}{r_i},$$
 (C.8)

$$cov(r_i, r_j) \simeq 0 \quad \text{for} \quad i \neq j,$$
 (C.9)

$$cov(\theta_i, \theta_i) \simeq 0 \quad \text{for} \quad i \neq j.$$
 (C.10)

We have supposed that the errors on each point coordinates are independent. Then we compute the mean radius and sine and cosine discrete Fourier series for the equations (assuming the point i=0 is the point i=N and i = N + 1 the point i = 1):

$$R = \frac{1}{2\pi} \sum_{i=1}^{N} \left(\frac{r_i + r_{i+1}}{2} \right) (\theta_{i+1} - \theta_i), \qquad (C.11)$$

$$a_{n} = \frac{1}{\pi R} \sum_{i=1}^{N} (r_{i} \cos(n\theta_{i}) + r_{i+1} \cos(n\theta_{i+1}) \frac{\theta_{i+1} - \theta_{i}}{2},$$

$$(C.12)$$

$$b_{n} = \frac{1}{\pi R} \sum_{i=1}^{N} (r_{i} \sin(n\theta_{i}) + r_{i+1} \sin(n\theta_{i+1}) \frac{\theta_{i+1} - \theta_{i}}{2},$$

$$(C.13)$$

which leads, for the variance, to

$$\begin{split} \sigma_R^2 &= \sum_{i=1}^N \left(\frac{\theta_{i+1} - \theta_{i-1}}{4\pi}\right)^2 2\sigma_0^2 + \sum_{i=1}^N \left(\frac{r_{i-1} - r_{i+1}}{4\pi}\right)^2 \frac{2\sigma_0^2}{r_i^2} \\ &+ \sum_{i=1}^N \frac{\theta_{i+1} - \theta_{i-1}}{4\pi} \frac{r_{i-1} - r_{i+1}}{4\pi} \frac{2\sigma_0^2}{r_i}, \qquad (C.14) \\ \sigma_{a_n}^2 &= \sigma_{r_0}^2 \left(\frac{a_n}{R}\right)^2 + \sum_{i=1}^N \sigma_0^2 \left(\frac{1}{\pi R}\right)^2 \frac{\cos^2(n\theta_i)}{2} (\theta_{i+1} - \theta_{i-1})^2 \\ &+ \sum_{i=1}^N \frac{2\sigma_0^2}{r_i} \left(\frac{1}{\pi R}\right)^2 \left[-r_i n \sin(n\theta_i) \frac{\theta_{i+1} - \theta_{i-1}}{2} \right. \\ &- (r_{i+1} \cos(n\theta_{i+1}) - r_{i-1} \cos(n\theta_{i-1}) \frac{1}{2} \right]^2 \\ &+ 2 \sum_{i=1}^N \frac{\sigma_0^2}{4\pi} \left[\theta_{i+1} - \theta_{i-1} + \frac{r_{i-1} - r_{i+1}}{r_i} \right] \\ &\times \left(-\frac{a_n}{R} \right) \frac{1}{\pi R} \cos(n\theta_i) (\theta_{i+1} - \theta_{i-1}) \\ &+ 2 \sum_{i=1}^N \frac{\sigma_0^2}{4\pi r_i} \left[\theta_{i+1} - \theta_{i-1} + \frac{r_{i-1} - r_{i+1}}{r_i} \right] \\ &\times \left(-\frac{a_n}{R} \right) \frac{1}{\pi R} \left[-r_i n \sin(n\theta_i) \frac{\theta_{i+1} - \theta_{i-1}}{2} \right. \\ &- (r_{i+1} \cos(n\theta_{i+1}) - r_{i-1} \cos(n\theta_{i-1}) \frac{1}{2} \right] \\ &+ 2 \sum_{i=1}^N \frac{2\sigma_0^2}{r_i} \left(\frac{1}{\pi R} \right)^2 \frac{\cos(n\theta_i)}{2} (\theta_{i+1} - \theta_{i-1}) \\ &\times \left[-r_i n \sin(n\theta_i) \frac{\theta_{i+1} - \theta_{i-1}}{2} \right. \\ &- (r_{i+1} \cos(n\theta_{i+1}) - r_{i-1} \cos(n\theta_{i-1}) \frac{1}{2} \right] . \end{aligned}$$
 (C.15)

We compute similarly σ_{b_n} , and the covariances $cov(a_n, R)$, $\operatorname{cov}(b_n, R)$ and $\operatorname{cov}(a_n, b_n)$. With $c_n^2 = a_n^2 + b_n^2$, we have $q = n/\langle R \rangle$ and

$$\langle |u|^2 \rangle = \left(\langle |c_n|^2 \rangle - \langle |c_n| \rangle^2 \right) \frac{\pi}{2} \langle R \rangle^3 .$$
 (C.16)

Taking into account the average over M contours, we can compute the standard deviations and covariances, for $\langle R \rangle$, $\langle c_n \rangle$ and $\langle c_n^2 \rangle$. If j is the index over the number of contours,

$$\sigma_{\langle |c_n|^2 \rangle}^2 = \frac{1}{M^2} \sum_{j=1}^M \sigma_{c_n^2}^2$$
 (C.17)

The same equation holds for other variances and covariances. Eventually, we find

$$\sigma_q^2 = \frac{\sigma_R^2 n^2}{(R)^4} \,,$$
 (C.18)

$$\sigma_{\langle |u|^2 \rangle}^2 = \left(\frac{\pi}{2} \langle R \rangle^3\right)^2 \sigma_{\langle c_n^2 \rangle}^2$$

$$+ \left(\frac{\pi}{2} \langle R \rangle^3\right)^2 (2 \langle c_n \rangle)^2 \sigma_{\langle c_n \rangle}^2$$

$$+ \left(3 \left(\langle c_n^2 \rangle - \langle c_n \rangle^2\right) \pi / 2 \langle R \rangle^2\right)^2 \sigma_{\langle R \rangle}^2$$

$$-4 \langle c_n \rangle \left(\frac{\pi}{2} \langle R \rangle^3\right)^2 \operatorname{cov}(\langle c_n^2 \rangle, \langle c_n \rangle)$$

$$+ \langle R \rangle^3 \left(\langle c_n^2 \rangle - \langle c_n \rangle^2\right)$$

$$\times \frac{3\pi^2}{2} \langle R \rangle^2 \operatorname{cov}(\langle c_n^2 \rangle, \langle R \rangle)$$

$$- \langle c_n \rangle \pi^2 \langle R \rangle^3 3 \left(\langle c_n^2 \rangle - \langle c_n \rangle^2\right)$$

$$\times \langle R \rangle^2 \operatorname{cov}(\langle c_n \rangle, \langle R \rangle)$$
(C.19)

(see Fig. 6). In these equations, and in the next one, we do not write the index n which labels the mode number, but obviously, $\langle u^2 \rangle$, q, and their associated variances and covariances depend on n.

We find the variances on the bending modulus κ and the tension σ following reference [57], pp. 458-460. We write the amplitude as

$$\langle |u|^2 \rangle = f(q, \sigma, \kappa),$$
 (C.20)

where f is given by equation (22). If k indexes the P modes (denoted previously by n) of the points (q_k, u_k) of the fluctuation spectrum,

$$\sigma_{\sigma}^{2} = \frac{\hat{K}}{|W|} \sum_{k} \left(\frac{\partial f}{\partial \kappa}\right)^{2} (q_{k}) \times g_{k}$$
 (C.21)

and

$$\sigma_{\kappa}^{2} = \frac{\hat{K}}{|W|} \sum_{k} \left(\frac{\partial f}{\partial \sigma}\right)^{2} (q_{k}) \times g_{k}, \qquad (C.22)$$

where

$$W = \begin{bmatrix} \sum_{k} \left(\frac{\partial f(q_{k})}{\partial \sigma} \right)^{2} g_{k} & \sum_{k} \frac{\partial f(q_{k})}{\partial \sigma} \frac{\partial f(q_{k})}{\partial \kappa} g_{k} \\ \sum_{k} \frac{\partial f(q_{k})}{\partial \sigma} \frac{\partial f(q_{k})}{\partial \kappa} g_{k} & \sum_{k} \left(\frac{\partial f(q_{k})}{\partial \kappa} \right)^{2} g_{k} \end{bmatrix},$$
(C.23)

$$\frac{1}{g_k} = \left[\sigma_{\langle |u|^2 \rangle}^2 + \left(\frac{\partial f}{\partial q_x} \sigma_q \right)^2 \right] \tag{C.24}$$

and

$$\hat{K} = \frac{1}{P-2} \sum_{k} g_k \left[\left\langle \left| u \right|^2 \right\rangle_k - f(q_k, \sigma, \kappa) \right]^2 . \quad (C.25)$$

We use Romberg integration method to compute numerically the derivatives of f. These equations are used to estimate the error reported in Table 1.

References

- 1. U. Seifert, Adv. Phys. 46, 13 (1997).
- 2. W. Helfrich, Z. Naturforsch. C 28, 693 (1973).
- 3. W. Helfrich, Z. Naturforsch. A 33, 305 (1978).
- 4. R.-M. Servuss, W. Harbich, W. Helfrich, Biochim. Biophys. Acta 436, 900 (1976).
- 5. P.B. Canham, J. Theor. Biol. 26, 61 (1970).
- J.B. Fournier, A. Ajdari, L. Peliti, Phys. Rev. Lett. 86, 4970 (2001).
- H.-G. Döbereiner, Curr. Opin. Colloid Interface Sci. 5, 256 (2000).
- B.M. Discher, Y.-Y. Won, D.S. Ege, J.C.-M. Lee, F.S. Bates, D.E. Discher, D.A. Hammer, Science 284, 1143 (1999).
- B.M. Discher, H. Bermudez, D.A. Hammer, D.E. Discher, Y.-Y. Won, F.S. Bates, J. Phys. Chem. B 106, 2848 (2002).
- P. Ratanabanangkoon, M. Gropper, R. Merkel, E. Sackmann, A.P. Gast, Langmuir 19, 1054 (2003).
- 11. E. Evans, W. Rawicz, Phys. Rev. Lett. 64, 2094 (1990).
- 12. L. Bo, R.E. Waugh, Biophys. J. 55, 509 (1989).
- 13. M. Kummrow, W. Helfrich, Phys. Rev. A 44, 8356 (1991).
- F. Brochard, J.-F. Lennon, J. Phys. (Paris) 36, 1035 (1975).
- M.A. Peterson, H.H. Strey, E. Sackmann, J. Phys. II 2, 1273 (1992).
- S. Tuvia, A. Almagor, A. Bitler, S. Levin, R. Korenstein,
 S. Yedgar, Proc. Natl. Acad. Sci. U.S.A. 94, 5045 (1997).
- A.Yu. Krol, M.G. Grinfeldt, S.V. Levin, A.D. Smilgavichus, Eur. Biophys. J. 19, 93 (1990).
- C.H. Lee, W.C. Lin, J. Wang, Phys. Rev. E 64, 020901 (2001).
- M.B. Schneider, J.T. Jenkins, W.W. Webb, J. Phys. 45, 1457 (1984).
- I. Bivas, P. Hanusse, P. Bothorel, J. Lalanne, O. Aguerre-Chariot, J. Phys. (Paris) 48, 855 (1987).
- H.H. Strey, M.A. Peterson, E. Sackmann, Biophys. J. 69, 478 (1995).
- 22. M. Mutz, W. Helfrich, J. Phys. (Paris) 51, 991 (1990).
- H. Engelhardt, H.-P. Duwe, E. Sackmann, J. Phys. (Paris) Lett. 46, 395 (1985).
- J.F. Faucon, M.D. Mitov, P. Méléard, I. Bivas, P. Bothorel,
 J. Phys. (Paris) 50, 2389 (1989).
- M.D. Mitov, J.F. Faucon, P. Méléard, P. Bothorel, Thermal fluctuations of membranes in Advances in Supramolecular Chemistry, edited by G.W. Gokel, Vol. 2 (Jai Press, Greenwich, CT, 1992) pp. 93-139.
- P. Méléard, C. Gerbeaud, T. Pott, L. Fernandez-Puente,
 I. Bivas, M.D. Mitov, J. Dufourcq, P. Bothorel, Biophys.
 J. 72, 2616 (1997).
- W. Häckl, U. Seifert, E. Sackmann, J. Phys. II 7, 1141 (1997).
- H.-P. Duwe, J. Käs, E. Sackmann, J. Phys. (Paris) 51, 945 (1990).
- H.-G. Döbereiner, E. Evans, M. Kraus, U. Seifert, M. Wortis, Phys. Rev. E 55, 4458 (1997).
- H.-G. Döbereiner, G. Gompper, C.K. Haluska, D.M. Kroll,
 P.G. Petrov, K.A. Riske, Phys. Rev. Lett. 91, 048301 (2003).
- 31. T. Pott, P. Méléard, Europhys. Lett. 59, 87 (2002).
- 32. J. Prost, R. Bruinsma, Europhys. Lett. 33, 321 (1996).
- S. Ramaswamy, J. Toner, J. Prost, Phys. Rev. Lett. 84, 3494 (2000).

- J.-B Manneville, P. Bassereau, S. Ramaswamy, J. Prost, Phys. Rev. E 64, 021908 (2001).
- M.I. Angelova, D.S. Dimitrov, Mol. Cryst. Liq. Cryst. 152, 89 (1987).
- M.I. Angelova, S. Soléau, P. Méléard, J.F. Faucon, P. Bothorel, Prog. Colloid Polym. Sci. 89, 127 (1992).
- 37. L. Mathivet, S. Cribier, P. F. Devaux, Biophys. J. **70**, 1112 (1996).
- 38. P. Méléard, J.F. Faucon, M.D. Mitov, P. Bothorel, Europhys. Lett. 19, 267 (1992).
- 39. P. Nassoy, private communication (2000).
- H.-G. Döbereiner, Fluctuating vesicle shapes, in Perspectives in Supramolecular Chemistry, edited by P.L. Luisi,
 P. Walde, Giant vesicles, Vol. 6 (John Wiley and Sons, Chichester, 2000).
- P. Méléard, C. Gerbeaud, P. Bardusco, N. Jeandaine, M.D. Mitov, L. Fernandez-Puente, Biochimie 80, 401 (1998).
- 42. C. Gerbeaud, PhD Thesis, University Bordeaux I (1998).
- S. Inoué, K.R. Spring VideoMicroscopy The Fundamentals, second edition (Plenum Press, New York, 1997).
- 44. T. Wilson, C.J.R. Sheppard, Optik 59, 19 (1981).
- 45. M. Gu, Advanced Optical Imaging Theory, in Optical Sciences (Springer, Berlin, 2000).

- 46. S. Inoué, Methods Cell Biol. 30, 85 (1989).
- 47. W.H. Press, W.T. Vetterling, S.A. Teukolsky, B.P. Flannery, *Numerical Recipes in C, the Art of Scientific Computing*, second edition (Cambridge University Press, Cambridge, 1992).
- 48. S.T. Milner, S.A. Safran, Phys. Rev. A 36, 4371 (1987).
- W. Helfrich, R.-M. Servuss, Nuovo Cimento D 3, 137 (1984).
- 50. C. Cohen-Tannoudji, B. Diu, F. Laloë, *Mécanique Quantique I* (Hermann, Paris, 1973).
- 51. S. Ramaswamy, Physica A 186, 154 (1992).
- L.D. Landau, E.M. Lifschitz, Mécanique des fluides, in Physique théorique, Vol. 6 (Editions Mir, Moscou, 1989).
- F. Gittes, B. Mickey, J. Nettleton, J. Howard, J. Cell Biol. 120, 923 (1993).
- 54. J.R. Henriksen, J.H. Ipsen, Eur. Phys. J. E 9, 365 (2002).
- 55. R.C. Weast (Editor), Handbook of Chemistry and Physics, 69th edition (CRC Press, Boca Raton, 1988).
- 56. J. Song, R.E. Waugh, Biophys. J. 64, 1967 (1993).
- M. Neuilly, CETAMA, Modélisation et Estimation des Erreurs de Mesure, second edition (Lavoisier, Tec et Doc, Paris, 1998).